Nano Research

Open Access

Research Article

Undercoordination engineering of chromium single-atom catalyst with optimized d-p hybridization for lithium-sulfur batteries

Hongyang Li[1,§], Jianjun Zhang[1,§], Yingrui Ding[1], Zhanpeng Huang[1], Pengsen Qian[1], Fanyang Sun[1], Huimin Wang[2] ✉, and Gaoran Li[1] ✉

[1] School of Materials Science and Engineering, Nanjing University of Science and Technology, Nanjing 210094, China
[2] Department of Applied Biology and Chemical Technology, The Hong Kong Polytechnic University, Hong Kong 999077, China
[§] Hongyang Li and Jianjun Zhang contributed equally to this work.

Cite this article: *Nano Research*, **2026**, *19*, 94907915. https://doi.org/10.26599/NR.2025.94907915

ABSTRACT: Sluggish sulfur redox kinetics remain a critical bottleneck in the advancement of high-performance lithium-sulfur batteries (LSBs). Single-atom catalysts (SACs) offer a promising solution to this limitation, particularly when their coordination structures are carefully engineered. Here, we develop a chromium-based SAC featuring a unique undercoordinated CrN_3 configuration to boost sulfur electrochemistry. Compared with conventional CrN_4, the CrN_3 motif lowers 3d orbital occupancy and meanwhile activates the in-plane hybridizations with S 3p orbitals upon interaction with polysulfides, contributing to moderate adsorption strength and reduced energy barriers for bidirectional sulfur conversions. Additionally, the integration of the two-dimensional (2D) porous framework ensures abundant electrochemically active surfaces and efficiently exposed active sites. As a result, CrN_3-based cells demonstrate fast and durable sulfur redox reactions, enabling an ultralow capacity decay of 0.0075% per cycle over 1000 cycles and a high-rate capability of 651.9 mAh·g^{-1} at 5 C. The CrN_3 catalyst retains robust catalytic efficiency under demanding conditions, delivering a high areal capacity of 5.53 mAh·cm^{-2} at high sulfur loading and lean electrolyte. This work establishes a compelling paradigm of SAC coordination engineering for designing advanced sulfur electrocatalysts for next-generation LSBs.

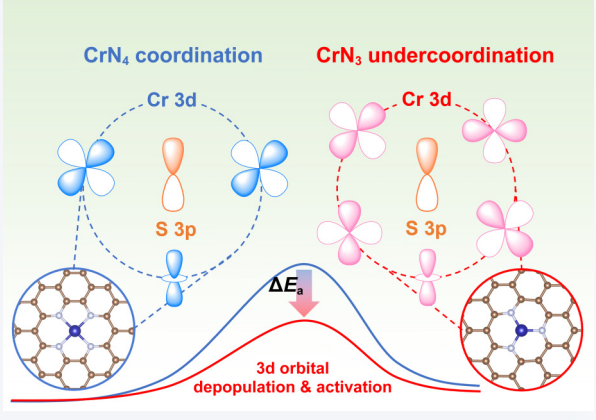

KEYWORDS: lithium-sulfur batteries, single-atom catalysts, coordination structure, orbital hybridization, sulfur electrocatalysis

1 Introduction

With the rapid expansion of electronics and electric vehicle markets, conventional lithium-ion batteries (LIBs) are increasingly constrained by their limitations in energy density and cost for meeting rising energy demands. Among emerging alternatives, lithium-sulfur batteries (LSBs) have attracted significant attention due to their exceptionally high theoretical capacity (1675 mAh·g^{-1}) and energy density (2600 Wh·kg^{-1}) [1–4]. In addition, sulfur's abundance, wide geographical availability, low cost, and environmental benignity render LSBs particularly appealing for large-scale applications [5, 6]. Despite these advantages, the practical implementation of this technology is hindered by fundamental challenges. The dissolution and diffusion of intermediate lithium polysulfides (LPSs) trigger the notorious "shuttle effect", leading to active material loss and electrode passivation. Moreover, the insulating nature of sulfur and its lithiation products, coupled with the complex multi-electron, multi-phase conversion mechanism, determines the sluggish sulfur redox kinetics. These issues collectively result in low reaction efficiency, limited cycle life, and poor rate capability [7–9].

Over the past decades, extensive research has focused on developing advanced sulfur electrocatalysts to address these persistent challenges [10–12]. Carbon-based materials have been widely studied owing to their high conductivity and lightweight characteristics [13, 14]. Nevertheless, the inherently weak sulfur

Received: June 18, 2025; **Revised:** August 5, 2025
Accepted: August 12, 2025

✉Address correspondence to Huimin Wang, hm-polyu.wang@polyu.edu.hk; Gaoran Li, gaoranli@njust.edu.cn

affinity limits their catalytic activity, often necessitating functional modifications such as heteroatom doping (e.g., N, P, and S) [15]. Apart from that, polar metal compounds like oxides [16, 17], sulfides [18], and phosphides [19], exhibit stronger interactions with LPSs and enhanced electrocatalytic activity, but typically suffer from poor conductivity and limited exposure of active sites. Metal-organic frameworks (MOFs) and covalent-organic frameworks (COFs), with highly ordered architectures and high porosity, offer promising platforms for sulfur confinement, yet their limited charge transfer efficiency hampers redox kinetics [20–22]. Recently, single-atom catalysts (SACs) have emerged as compelling alternatives [23, 24]. Featuring atomically dispersed active sites, SACs ensure maximum metal utilization and exceptional catalytic efficiency. Beyond that, their well-defined local structure enables precise modulations of electronic structures and interaction behaviors with LPSs, presenting a powerful avenue to break the bottleneck in sulfur electrocatalysis.

The rational selection of central metals is crucial in designing SACs for LSBs [25]. Compared with noble-metal SACs, those based on 3d transition metals (TM-SACs) offer a more cost-effective and practical approach. First-principles calculations have revealed that the interactions between TM-SACs and LPSs primarily occur through the M–S bonding, governed by the Lewis acid-base principle. These behaviors are dictated by the hybridization between TM 3d and S 3p orbitals, where the electronic structure of the hybridized states determines the bonding strength and catalytic activity for sulfur redox [26]. Generally, late 3d TMs, with mostly filled 3d orbitals, provide limited empty states to accept electrons from sulfur, resulting in weak LPS adsorption. In comparison, group VIII TMs (e.g., Fe, Co, Ni), with partially filled 3d orbitals, offer superior electron acceptance and exhibit stronger M–S interaction with good catalytic activity [27], making them widely studied. Further extending this trend, early 3d TMs such as V and Ti, with lower 3d orbital occupancy, provide abundant empty orbitals and demonstrate the highest-level LPS adsorbability among TM-SACs. However, excessively strong LPS fixation may hinder electrocatalytic performance by disrupting the balance among adsorption, diffusion, and desorption, ultimately impairing overall sulfur redox kinetics.

Considering these factors, chromium stands out as a promising candidate, situated at the boundary between early- and mid-TMs in the periodic table. Its moderate 3d electron density enables a balanced electronic interaction with LPSs, facilitating optimized adsorption and catalytic performance. Despite this potential, Cr-SACs remain largely unexplored in LSBs to date. Beyond that, the local coordination environment also plays a critical role in governing the catalytic behavior of SACs. Conventional SACs typically adopt a symmetric MN_4 configuration, in which the metal center is surrounded by four nitrogen atoms, corresponding to a coordination number (CN) of four. While this configuration offers favorable thermodynamic stability, it does not translate into optimal catalytic performance. Recent studies have demonstrated that modulating the coordination number, either through overcoordination (CN > 4) or undercoordination (CN < 4), can finely alter the electronic structure and optimize the SACs-LPSs interactions, thereby enhancing catalytic activity [28].

In this contribution, we developed a unique undercoordinated Cr single-atom catalyst (denoted as CrN_3) to enhance sulfur redox efficiency and kinetics in LSBs. The CrN_3 catalyst was synthesized employing a Cr-impregnated layered zeolitic imidazolate framework (Cr@ZIF-L) as a precursor, yielding atomically dispersed Cr sites anchored on a nitrogen-rich, porous, and two-dimensional (2D) carbon matrix. Compared to conventional CrN_4, the undercoordination in CrN_3 increases Cr 3d electron density and activates the Cr d_{xy} and $d_{x^2-y^2}$ orbitals upon hybridization with S 3p orbitals, leading to moderately weakened LPS adsorption but significantly reduced energy barriers for bidirectional sulfur conversions. This favorable correlation between coordination environment and catalytic behaviors was systematically investigated and validated through extensive theoretical calculations, physicochemical characterizations, and electrochemical evaluations. As a result, CrN_3-based LSBs demonstrated accelerated and reversible sulfur electrochemistry, delivering outstanding cycling stability and rate capability that significantly outperformed their CrN_4 counterparts. Moreover, robust electrochemical performance was maintained even under demanding conditions, including high sulfur loading (5.5 $mg \cdot cm^{-2}$) and limited electrolyte (5.0 $mL \cdot g^{-1}$), underscoring the great potential of this undercoordination engineering for advancing high-performance and practically viable LSBs.

2 Results and discussion

Figure 1(a) schematically illustrates the preparation of CrN_4 and CrN_3. Particulate ZIF-8 and leaf-like ZIF-L were obtained by assembling Zn^{2+} and 2-methylimidazole in methanol and aqueous media, respectively, upon which Cr ions were *in situ* impregnated into these frameworks (Cr@ZIF-8 and Cr@ZIF-L). Subsequent pyrolysis under an Ar atmosphere produced CrN_4 with conventional coordination and CrN_3 with undercoordination. Scanning electron microscopy (SEM) images reveal the morphological evolution throughout the synthesis. As shown in Figs. S1 and S2 in the Electronic Supplementary Material (ESM), ZIF-L exhibits a well-defined leaf-like morphology with a smooth surface and a thickness of around 130 nm, which becomes notably rougher upon Cr impregnation while well retaining its 2D structure. After high-temperature pyrolysis, the leaf-like micromorphology is preserved but becomes more porous and loosely structured (Fig. 1(b) and Fig. S3 in the ESM). Energy-dispersive X-ray spectroscopy (EDS) mapping confirms the uniform distribution of C, N, and Cr in CrN_3, manifesting successful carbonization and Cr incorporation into the N-doped carbon matrix (Fig. 1(c)). Transmission electron microscopy (TEM) image further reveals the layered leaf-like architecture with abundant meso- and micro-pores (Fig. 1(d)), which are beneficial for facilitating charge/mass transfer and exposing active sites for catalytic processes. High-angle annular dark field-scanning transmission electron microscope (HADDF-STEM) image identifies atomically dispersed bright spots (yellow circled) throughout the matrix, confirming the existence of Cr single atoms in the as-prepared CrN_3 (Fig. 1(e)). For comparison, CrN_4 was prepared using Cr@ZIF-8 as the precursor, which retained a typical polyhedral morphology in uniform particle size after carbonization, with Cr single atoms similarly identified by HADDF-STEM (Figs. 1(f)–1(i) and Fig. S4 in the ESM). The Cr contents in CrN_3 and CrN_4 were determined to be 1.30 wt.% and 1.23 wt.%, respectively, as measured by inductively coupled plasma (ICP) analysis. In addition, bare N-doped carbon (NC) was also obtained by carbonizing ZIF-L without Cr-impregnation, showing a similar 2D leaf-like architecture (Fig. S5 in the ESM).

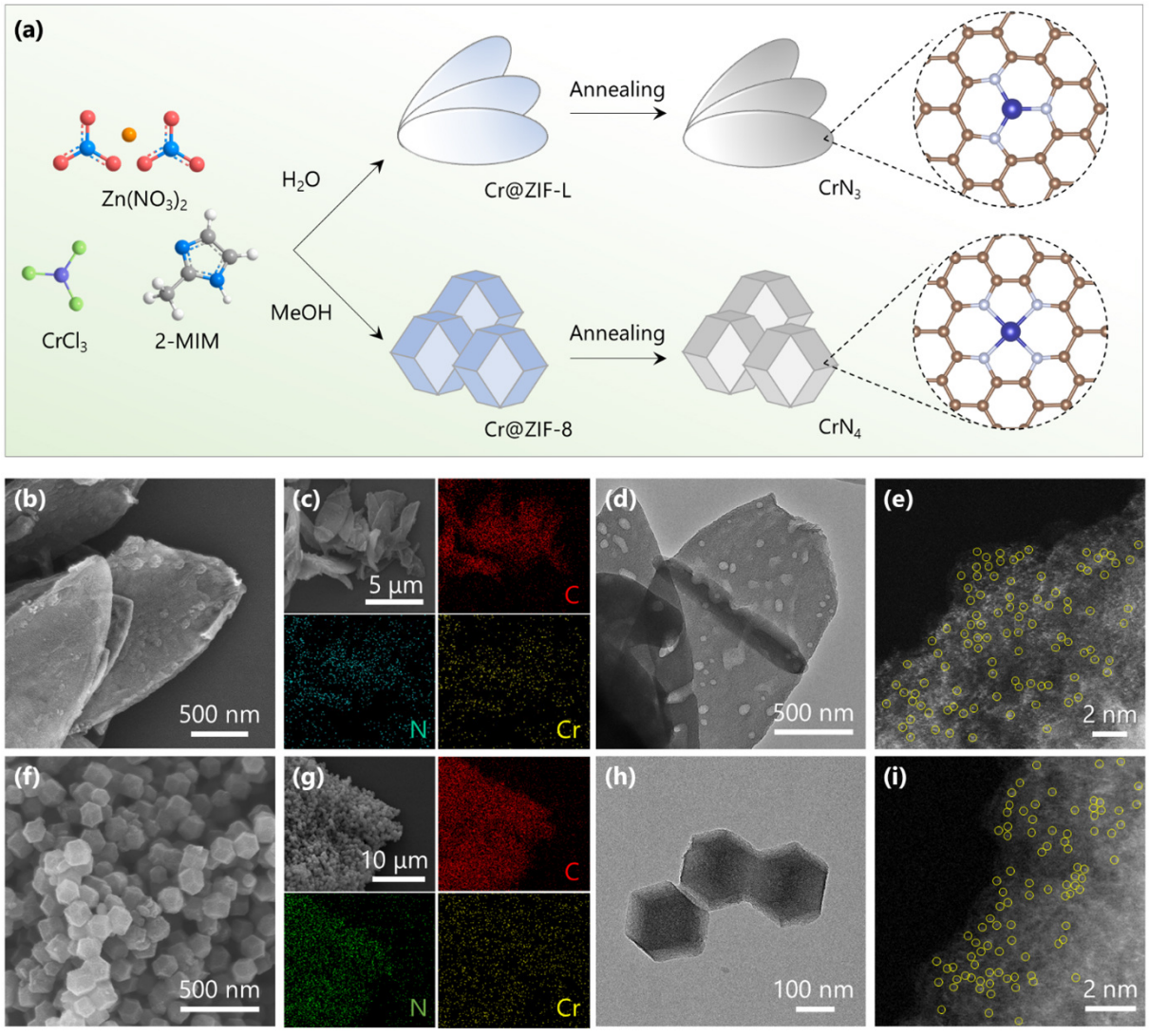

Figure 1 (a) Schematic preparation of CrN_3 and CrN_4. (b) SEM, (c) EDS mapping, (d) TEM, and (e) AC-HAADF-STEM images of CrN_3. (f) SEM, (g) EDS mapping, (h) TEM, and (i) AC-HAADF-STEM images of CrN_4.

The phase and crystalline evolution during synthesis were investigated using X-ray diffraction (XRD). As shown in Fig. S6 in the ESM, the Cr-impregnation does not significantly alter the crystalline structures of either ZIF-8 or ZIF-L, aligning the well-preserved morphologies observed in SEM. After pyrolysis, the XRD patterns of CrN_3, CrN_4, and NC all demonstrate typical amorphous character with a broad band at around 26°, confirming the complete decomposition and carbonization of ZIF precursors. Importantly, no characteristic peaks associated with Cr species were detected, suggesting the atomic dispersion of Cr in both CrN_3 and CrN_4, consistent with the HAADF-STEM findings. Given the SEM and TEM observations, N_2 adsorption–desorption measurement was carried out to further characterize the porous texture. CrN_3 and CN exhibit typical type-I curves, indicative of their dominance by micropores, while CrN_4 displays a type-II curve, suggesting a higher proportion of mesopores (Fig. 2(a)). The specific surface areas of CrN_3, CrN_4, and NC were measured to be 773.84, 966.41, and 998.38 $m^2 \cdot g^{-1}$, respectively. This distinction is further clarified by the pore size distributions in Fig. 2(b). Although mesopores generally benefit charge/mass transport, architectural factors should also be considered. To evaluate the electrochemically active surfaces of CrN_3 and CN_4, cyclic voltammetry (CV) was conducted at various scan rates. The slope from the linear fitting of current density versus scan rate (Fig. 2(c) and Fig. S7 in the ESM) is noted to be higher for CrN_3, indicating a larger electrochemically active surface area compared with its CrN_4 counterpart. This enhancement is attributed to the topological advantage of CrN_3's 2D layered structure, which reduces ion/electron diffusion distances and promotes efficient exposure of active surfaces, anticipated to translate into superior catalytic activity and efficiency. By contrast, the bulkier architecture of CrN_4 may restrict access to internal regions, limiting the overall utilization of active sites.

The local coordination environments of CrN_3 and CrN_4 were investigated using synchrotron radiation X-ray absorption spectroscopy. As shown in Fig. 2(d), the Cr K-edge X-ray absorption near-edge structure (XANES) spectra position the absorption edges of CrN_3 and CrN_4 between those of Cr foil and Cr_2O_3, with both leaning closer to the latter, suggesting the Cr valence close to +3 in these SACs. Notably, the slightly lower edge position of CrN_3 indicates a marginally reduced Cr valence state and, accordingly, a higher 3d electron density compared with CrN_4. Further insight can be gained from the pre-edge features (right inset

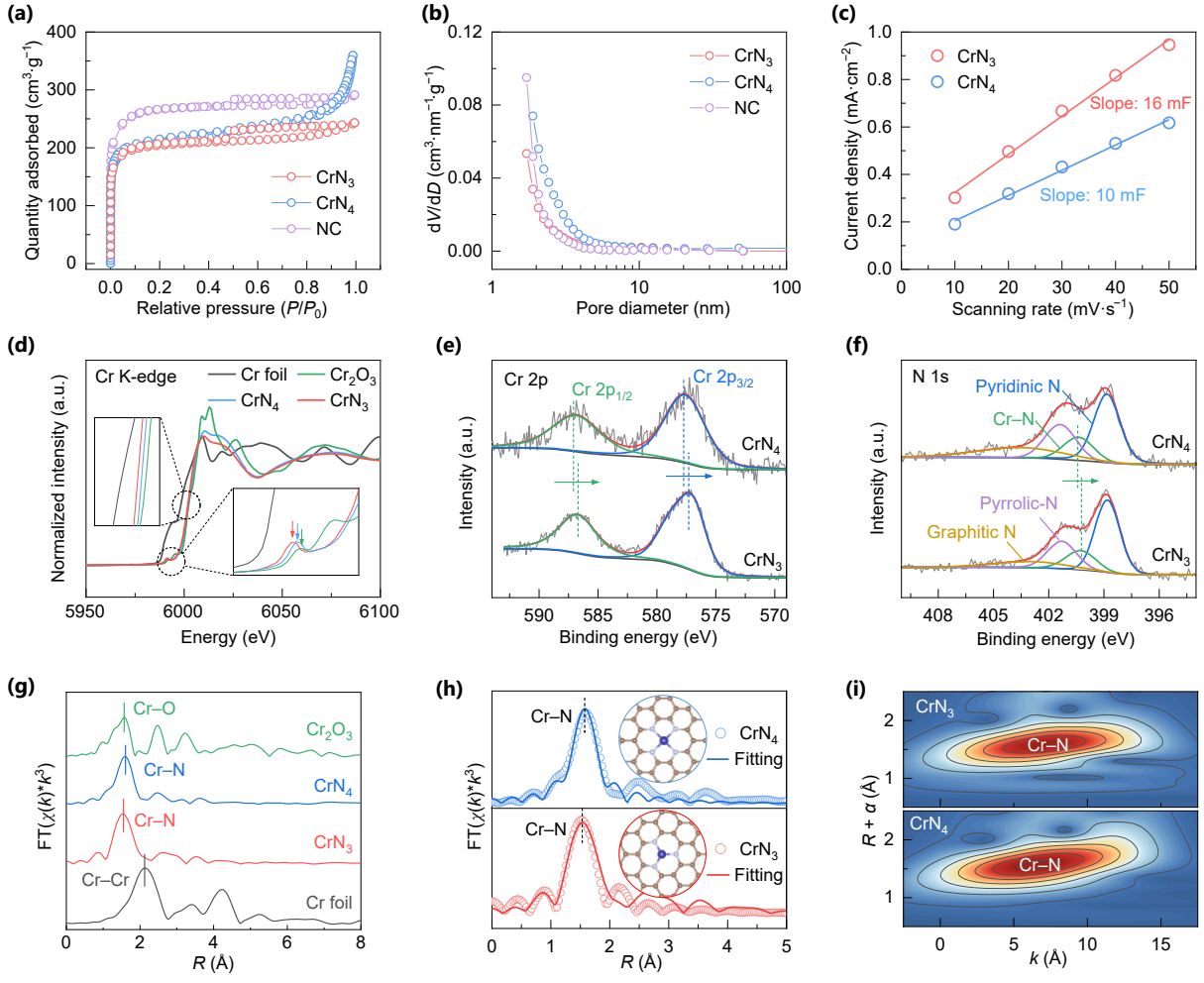

Figure 2 (a) N_2 adsorption–desorption isotherms and (b) pore size distributions of CrN_3, CrN_4, and NC; (c) linear fitting of current density versus CV scan rate for symmetric cells of CrN_3 and CrN_4; (d) Cr K-edge XANES; (e) Cr 2p XPS spectra; (f) N 1s XPS spectra; (g) k^3-weighted Fourier transformed EXAFS spectra and (h) the corresponding fitting in *R* space, and (i) WT-EXAFS spectra pf CrN_3 and CrN_4.

in Fig. 2(d)). CrN_3 exhibits a stronger pre-edge peak at lower energy than CrN_4 and Cr_2O_3, indicative of its reduced coordination symmetry and lower coordination number [29]. The electronic distinction in these two Cr-SAC systems can be also illustrated in X-ray photoelectron spectroscopy (XPS). CrN_3 witnesses the Cr 2p peak shifts toward a lower binding energy range compared to CrN_4 (Fig. 2(e)), manifesting its higher electron density and lower valence state. The N 1s XPS spectra provide additional insight into the local structure (Fig. 2(f)). Four subpeaks can be deconvoluted in both CrN_4 and CrN_3 spectra, indexed to pyridinic N (398.8 eV), pyrrolic N (401.3 eV), graphitic N (403.6 eV), and the metal–N bond (400.4 eV), respectively [30, 31]. Notably, the Cr–N peak for CrN_3 appears at a lower binding energy than that of CrN_4, suggesting stronger electron donation from Cr to N in CrN_3, despite the overall lower Cr valence.

Extended X-ray absorption fine structure (EXAFS) analysis was conducted to further probe into the local structures. As shown in Fig. 2(g), both CrN_3 and CrN_4 exhibit a prominent first-shell peak at approximately 1.6 Å in the k^3-weighed Fourier-transformed *R* space spectra, which can be attributed to the Cr–N scattering path, closely resembling the Cr–O path in Cr_2O_3. Crucially, no Cr–Cr scattering peak can be detected in either CrN_3 or CrN_4, confirming the atomically dispersed Cr and excluding the presence of metallic particles or oxide impurities, as further corroborated by the wavelet transformed (WT) EXAFS contour plots (Fig. 2(i) and Fig. S8 in the ESM). Quantitative EXAFS fitting in *R* space reveals an average coordination number to be approximately 4.0 for CrN_4 and 3.0 for CrN_3 (Table S1 in the ESM). Meanwhile, CrN_3 exhibits a slightly shorter Cr–N path compared with that in CrN_4 (1.87 vs. 2.01 Å), signifying stronger Cr–N bonding in the undercoordination structure consistent with the XPS results. Collectively, these findings confirm the successful synthesis of CrN_3 with a well-defined undercoordinated structure, accompanied by a finely modulated chemical state and electron density relative to the conventional CrN_4 structure.

Given this, the effect of coordinative modulation on sulfur electrochemistry was elucidated by density functional theory (DFT) calculations. The geometrically stable configurations of NC, CrN_4, and CrN_3 were modeled as shown in Fig. S9 in the ESM, with their corresponding polysulfide adsorptions illustrated in Figs. S10–S12 in the ESM. Representatively, Fig. 3(a) displays the adsorption geometry of Li_2S_4 on different catalysts. It is noted that Li bonding dominates the interaction between Li_2S_4 and NC, while strong Cr–S bonding is established on CrN_3 and CrN_4. These interactions are visualized via differential charge density patterns, where yellow and cyan regions refer to electron accumulation and depletion,

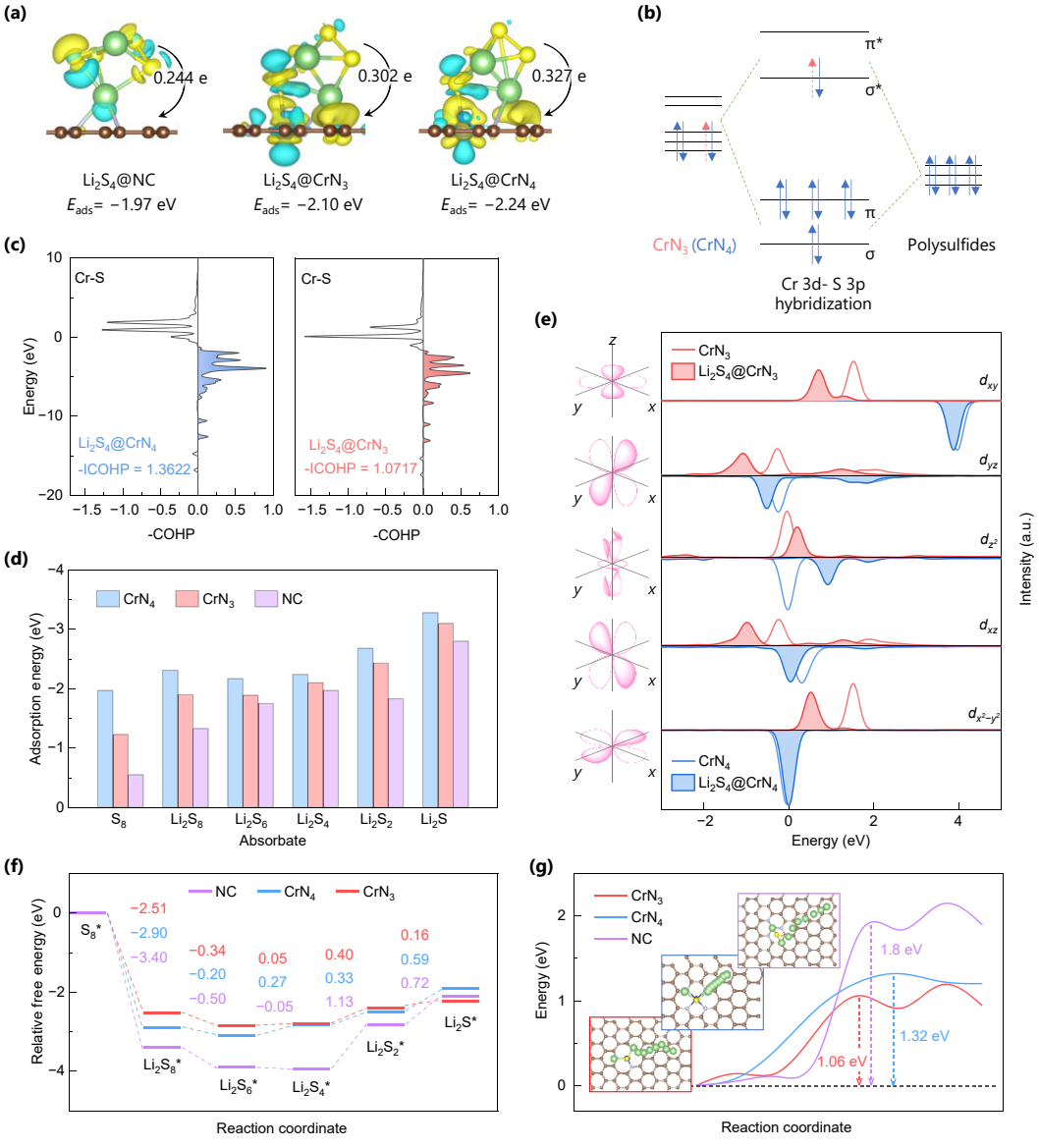

Figure 3 (a) Differential charge density and charge transfer upon Li_2S_4 adsorption on NC, CrN_3, and CrN_4. (b) Schematic for Cr 3d-S 3p orbital hybridization and (c) Cr-S COHP patterns upon Li_2S_4 adsorption on CrN_3 and CrN_4. (d) Adsorption energies of LPSs on different catalysts. (e) Cr 3d pDOS before and after Li_2S_4 adsorption on CrN_3 and CrN_4. (f) Gibbs free energy profiles of sulfur reduction and (g) energy barriers for Li_2S decomposition on different catalysts.

respectively. The Li_2S_4 adsorption energies are 1.75, 1.89, and 2.18 eV for NC, CrN_3, and CrN_4, respectively, aligning with their charge transfer (0.244e, 0.302e, and 0.327e) from Li_2S_4 to the catalytic surfaces. Despite both outperforming NC, CrN_3 is noted with slightly weaker adsorption than CrN_4, which should be attributed to the coordination-induced modulation in electronic structure. With less N-coordination, CrN_3 delivers a higher Cr 3d orbital occupation with a lower capability of accommodating S 3p electron donation upon the Cr 3d-S 3p hybridization (Fig. 3(b)). This trend is corroborated by the partial density of states (pDOS) of Cr d-band, as shown Fig. S13 in the ESM. According to the d-band center theory, a higher d-band center suggests an elevated energy level of the antibonding states formed upon hybridization with S 3p orbitals. This, in turn, promotes greater occupation of the bonding states, thereby enhancing the stability of the adsorption configuration. Accordingly, the higher d-band center of CrN_4 (−0.13 eV) than that of CrN_3 (−1.13 eV) contributes more significantly to the hybridized bonding state, leading to stronger adsorption of sulfur species. Consistently, the crystal orbital Hamilton population (COHP) analysis (Fig. 3(c)) reveals a less Cr–S bonding state of CrN_3 (–COHP = 1.0717) than that of CrN_4 (–COHP = 1.3622), confirming weaker polysulfide adsorption strength on the undercoordinated CrN_3 compared with that in the conventional CrN_4 scenario. This trend remains consistent across various LPSs, with CrN_3 showing slightly lower adsorption energies than CrN_4 but significantly higher than NC and electrolyte solvents (typically below 0.8 eV), as shown in Fig. 3(d).

According to Sabatier principle, excessively strong adsorption may impede product desorption and intermediate diffusion, ultimately limiting the overall reaction kinetics and catalytic efficiency. Therefore, a moderate interaction strength is preferred to balance adsorption and desorption for optimal catalytic activity. Beyond the occupation effect, the orbital orientation also plays a key role in the interactions between SACs and LPSs. In the case of

conventional CrN_4, the Cr–S bonding primarily arises from the hybridization between the vertical 3d orbitals of metal (i.e., d_{z^2} and $d_{xz/yz}$) and the 3p orbitals of sulfur, while the in-plane 3d orbitals ($d_{x^2-y^2}$ and d_{xy}) remain largely inactive, as illustrated by the significant (active) and negligible (inactive) change, respectively, in their pDOS patterns after Li_2S_4 adsorption (Fig. 3(e)), leading to a σ-dominant bonding mode. By contrast, the asymmetric undercoordination in CrN_3 activates the in-plane d_{xy} and $d_{x^2-y^2}$ orbitals, enabling significant pDOS change after polysulfide adsorption for all these orbital orientations, thus contributing to a σ, π dual-mode bonding upon the Cr-S p-d hybridization. The higher participation of π-bonds with enhanced electron delocalization would promote charge transfer and lower energy barriers for fast sulfur redox kinetics. Given this, Fig. 3(f) compares the Gibbs energy profiles of successive sulfur reduction reactions (SRR) on different catalytic surfaces. The undercoordination engineering shifts the rate-determining step from Li_2S_2-Li_2S for CrN_4 to Li_2S_4-Li_2S_2 in the CrN_3 scenario, with an energy barrier of 0.4 eV, significantly lower than both CrN_4 (0.59 eV) and NC (1.13 eV). Moreover, sulfur evolution reaction (SER) was also investigated with a focus on the oxidative dissociation of Li_2S (Fig. 3(g)). CrN_3 demonstrates the lowest energy barrier (1.06 eV) for Li–S bond cleavage and Li^+ diffusion, compared with those on CrN_4 (1.32 eV) and NC (1.8 eV). These results collectively underscore the significant superiority of undercoordination engineering in boosting both SRR and SER kinetics, offering a compelling strategy for enhancing sulfur electrocatalysis.

To validate the LPS anchoring capability, a static adsorption test was conducted by immersing catalysts in Li_2S_6 solutions and monitoring the color change (inset of Fig. 4(a)). Both CrN_3 and CrN_4 decolorized the solution significantly, in sharp contrast to the negligible change observed with NC and super P (SP), confirming their superior LPS adsorbability. This enhancement was further verified by ultraviolet–visible (UV–vis) spectroscopy, where Cr-SACs exhibited markedly reduced absorbance intensities near 290 and 420 cm^{-1}, which correspond to S_6^{2-} and S_4^{2-} species, respectively [32]. Notably, the CrN_3 specimen retains a slightly stronger absorbance than CrN_4, indicating a relatively weaker LPS adsorption consistent with the DFT prediction. The underlying chemical interaction was further investigated by XPS. As shown in Fig. 4(b), the S 2p spectrum of pristine Li_2S_6 exhibits typically two doublets referring to terminal sulfur (S_T^{-1}, 161.4 eV) and bridging sulfur (S_B^0, 163.1 eV), respectively. After adsorption on CrN_3, these peaks shift to a higher energy range accompanied by the emergence of a new band at around 168.6 eV associated with thiosulfate/sulfate species [33], indicating the partial oxidation and electron-donating

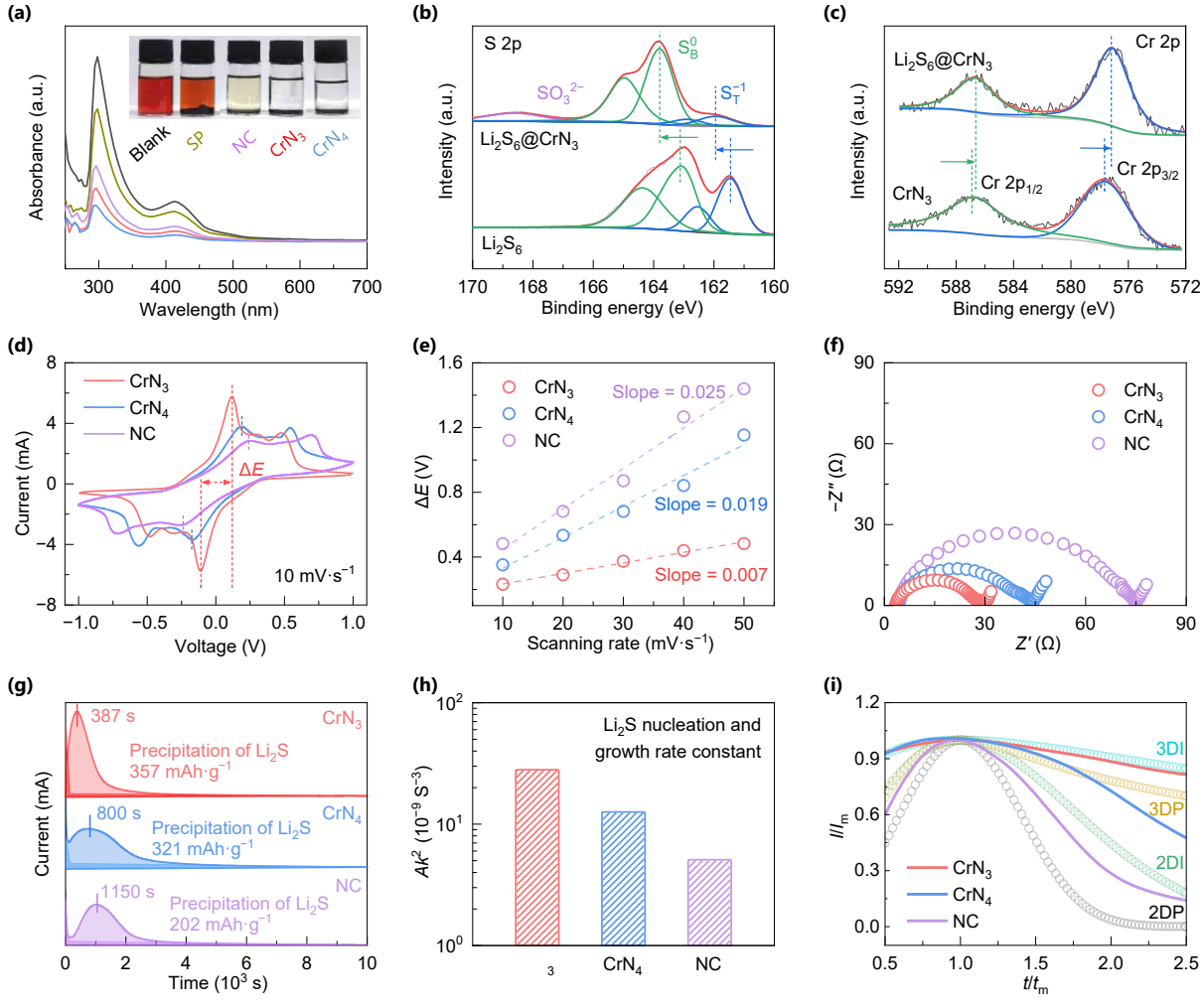

Figure 4 (a) UV–vis spectra of Li_2S_6 solution adsorbed by various catalysts with the inset showing the color difference after the adsorption. (b) S 2p and (c) Cr 2p XPS spectra before and after Li_2S_6 adsorption on CrN_3. (d) CV profiles, (e) redox peak gaps along the increase of scan rate, and (f) Nyquist plots of symmetric cells based on different catalysts. (g) Li_2S precipitation profiles, (h) Li_2S nucleation and growth rate constant, and (i) dimensionless transient of precipitation profiles on different catalysts.

character of sulfur upon polysulfide adsorption. Meanwhile, the Cr 2p peaks exhibit a negative shift after the adsorption, manifesting the electron acceptance of Cr, consistent with the classic Lewis acid-base principle and the DFT results [34].

The catalytic performance was further evaluated via CV measurements in symmetric cells. As shown in Fig. 4(d), the CrN_3 cell exhibits the highest current peak intensity and the smallest redox polarization, indicating its most rapid and efficient bidirectional LPS conversions. CV profiles at various scanning rates were collected (Fig. S14 in the ESM), with the evolution of redox potential gaps (ΔE) presented in Fig. 4(e). The CrN_3 cell consistently displays the smallest ΔE and the slowest ΔE increases with increasing scan rates, further highlighting its superior LPS conversion kinetics. Electrochemical impedance spectroscopy (EIS) also shows the lowest internal resistance of the CrN_3 cell (Fig. 4(f)), demonstrating its excellent charge transfer characteristics. Moreover, Li_2S precipitation, a generally acknowledged kinetic bottleneck in sulfur electrochemistry, was studied by potentiostatic measurement (Fig. 4(g)). CrN_3 enables the earliest reduction peak (387 s), the highest current response, and the largest precipitation capacity (357 mAh·g^{-1}), surpassing those of CrN_4 (800 s, 321 mAh·g^{-1}) and NC (1150 s, 202 mAh·g^{-1}). Correspondingly, the highest Li_2S nucleation and growth rate constant was obtained by CrN_3 (Fig. 4(h)). The Li_2S precipitation behaviors were further assessed according to the Bewick-Fleischmann-Thirsk and Scharifker-Hills models (Fig. 4(i)) [35]. The CrN_3 electrode aligns well with the three-dimensional instantaneous (3DI) growth mode, indicative of rapid and spatially uniform Li_2S nucleation and growth along both lateral and vertical directions. In contrast, CrN_4 and NC follow mixed 3D progressive/2D instantaneous (3DP/2DI) and 2DI/2DP modes, respectively, which are typically associated with planar Li_2S film formation that tends to block catalytic interfaces and hinder ion/electron transport. Collectively, these results strongly confirm the superior catalytic activity of undercoordinated CrN_3 in promoting both SSR and SER kinetics.

Based on the above results, coin cells were assembled to evaluate the practical catalytic performance in LSBs. As shown in Fig. 5(a), the CV profiles of all cells exhibit two distinct cathodic peaks and two partially overlapped anodic peaks, assigned to the stepwise reduction of element sulfur to soluble LPSs and further into insoluble Li_2S, as well as their subsequent reoxidation during reverse scanning [36]. It is noteworthy that the CrN_3 cell delivers the highest peak currents and narrowest potential gaps between redox peaks, indicating enhanced redox kinetics and reduced electrochemical polarization. This improvement was further quantified using Tafel slope analysis at different conversion steps (marked in the CV profiles). The CrN_3 cell shows consistently the lowest Tafel slopes among these samples (Fig. S15 in the ESM), confirming its superior facilitation of sulfur redox reactions. The activation energy barriers of these redox steps were calculated using a modified Arrhenius equation (Table S2 in the ESM) [37]. As shown in Fig. 5(b), CrN_4 reduces the energy barrier for the S_8-to-Li_2S_x, Li_2S_x-to-Li_2S, and Li_2S-to-Li_2S_x steps by 16.91, 19.13, and 25.91 kJ·mol^{-1}, respectively, compared with NC. Remarkably, CrN_3 achieves even lower barriers, further demonstrating the superiority of undercoordination engineering in boosting both SRR and SER kinetics. Considering Li^+ transfer property as another critical contributor to kinetic performance, CV profiles at varying scan rates were also recorded (Figs. 5(c) and 5(d), and Fig. S16 in the ESM), and the peak currents at different steps (peak I, II, and III) were plotted as a function of the square root of the scan rate to estimate Li^+ diffusion coefficients according to the Randles-Sevcik formula (Fig. 5(e) and Fig. S17 in the ESM) [38]. The CrN_3 cell demonstrates the highest fitting slope across all peaks, manifesting the fastest Li^+ diffusion. EIS measurement was also conducted to further probe the kinetic characteristics (Figs. 5(f) and 5(g), and Fig. S18 in the ESM). The CrN_3 cell exhibits the smallest semicircle at the high-medium frequency, indicative of its lowest charge-transfer resistance. By linearly fitting the temperature-dependent resistance based on the Arrhenius equation (Fig. S19 in the ESM) [39], the CrN_3 cell was proven to possess the lowest activation energy for charge transfer (26.1 kJ·mol^{-1}), in comparison with CrN_4 (36.5 kJ·mol^{-1}) and NC (40.3 kJ·mol^{-1}). These findings conclusively demonstrate the kinetic enhancement by the undercoordination engineering.

Galvanostatic charge–discharge measurements were carried out to evaluate the cycling performance of LSBs employing different catalysts. As shown in Fig. 6(a), all cells exhibit a typical two-plateau discharge profile and extended charging slope, corresponding to the multi-step sulfur redox reactions. Notably, the CrN_3 cell delivers an initial capacity of 1235.8 mAh·g^{-1} that significantly surpasses CrN_4 (1104.8 mAh·g^{-1}) and NC (983.8 mAh·g^{-1}) at 0.2 C, indicating a higher sulfur utilization. Moreover, a larger low-to-high plateau capacity ratio (Q_L/Q_H) of 2.3 is obtained for CrN_3 compared with CrN_4 (2.0) and NC (2.15), suggesting that the soluble LPSs generated at the upper plateau can be more efficiently reutilized and precipitated as solid Li_2S during the lower-plateau stage. Meanwhile, CrN_3 also demonstrates the smallest potential gap (ΔE) between charge and discharge curves, indicative of minimized polarization. The galvanostatic intermittent titration technique (GITT) further illustrates the kinetic feature during cycling. The instantaneous voltage drops (IR drops), referring to the deviation of working potential from equilibrium upon current interruption, were extracted across the depth of charge and discharge (Fig. S20 in the ESM). Among all the cells, CrN_3 enables consistently the smallest IR drop throughout the cycling range, highlighting its superior capability of mitigating overpotential and facilitating fast SRR and SER processes.

Figure 6(c) compares the cycling capacities of different cells at 0.2 C. The CrN_3 cell retains a capacity of 1116.4 mAh·g^{-1} after 100 cycles, much higher than those of the CrN_4 (952.8 mAh·g^{-1}) and NC (776.3 mAh·g^{-1}) cells, alongside nearly 100% Coulombic efficiency, indicating excellent redox reversibility and effective suppression of the shuttle effect. The cells were also subjected to continuous cycling at varying current rates to evaluate rate capability, with the corresponding voltage profiles presented in Fig. 6(d) and Fig. S21 in the ESM. Notably, the CrN_3 cell maintains well the two-plateau discharge profile even at a high rate of 5 C, while the CrN_4 and NC cells suffer from pronounced profile distortion accompanied by the disappearance of the second discharge plateau at high rates. Correspondingly, the CrN_3 cell delivers the smallest and slowest-growing redox potential gaps with the increasing current rates (Fig. 6(e)), further corroborating its superior catalytic activity and ability to sustain efficient redox reactions under high-rate conditions. As a result, the highest capacity of 651.9 mAh·g^{-1} is achieved by the CrN_3 cell at 5 C (Fig. 6(f)). When the current rate is reverted to 0.2 C, the CrN_3 cell recovers a capacity of 1050 mAh·g^{-1}, verifying its excellent electrochemical reversibility. Long-term cyclability was further investigated to validate the sustained catalytic advantage. As shown

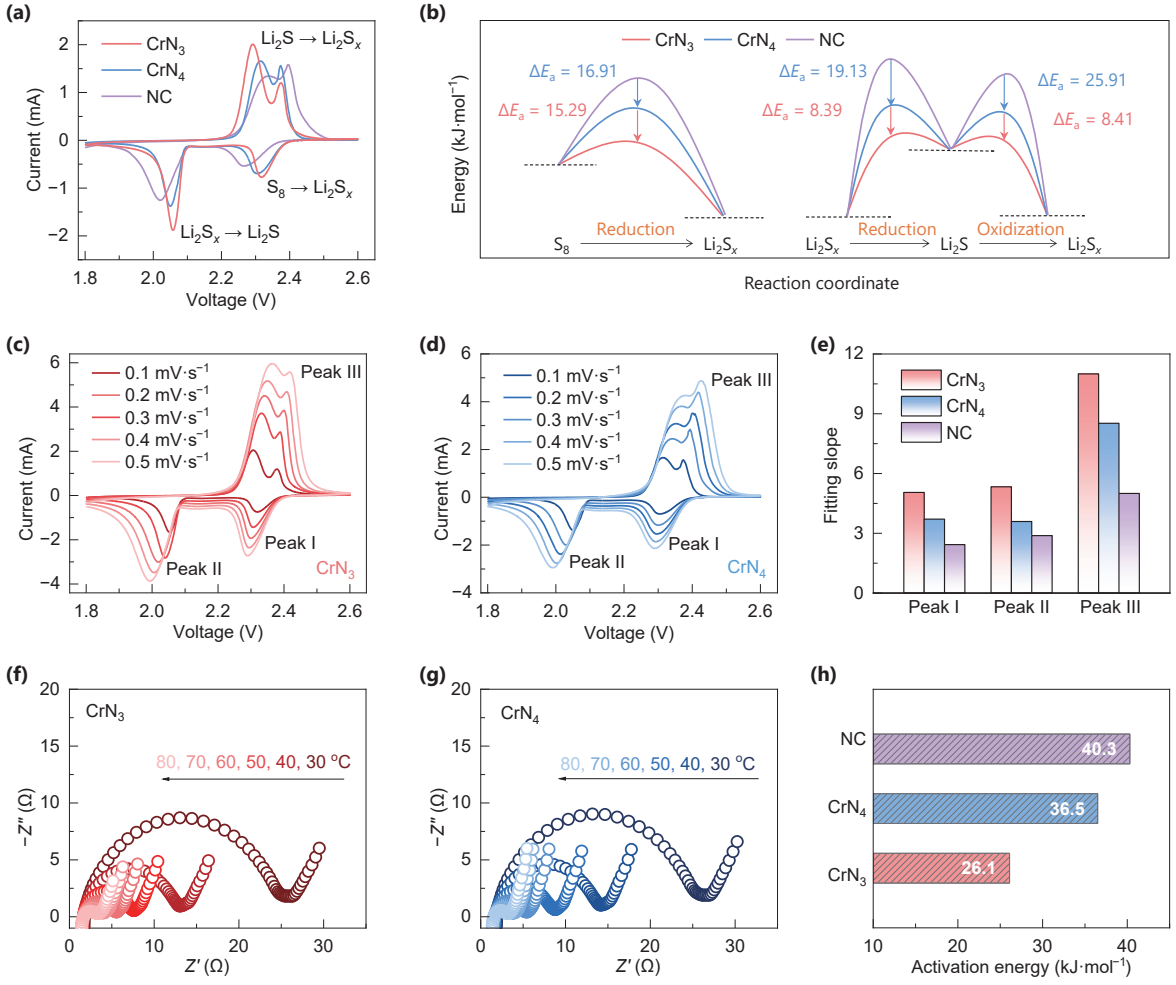

Figure 5 (a) CV profiles of LSBs based on CrN_3, CrN_4, and NC at 0.1 mV·s^{-1} and (b) the corresponding changes of activation energies at various conversion steps. CV profiles of (c) CrN_3 and (d) CrN_4 cells at various scan rates. (e) Linear fitting slopes of peak current density versus root of scan rate at different peaks in CV profiles. Nyquist plots of (f) CrN_3 and (g) CrN_4 cells at various temperatures, and (h) the calculated activation energies for charge transfer in different cells.

in Fig. S22 in the ESM, two distinct discharge plateaus can be maintained for both CrN_3 and CrN_4 cells throughout extended cycling, while CrN_3 consistently exhibits higher capacity retention and lower polarization. Specifically, the CrN_3 cell retains a capacity of 883.0 mAh·g^{-1} after 1000 cycles at 1 C with a minimal fading rate of only 0.0075% per cycle, significantly outperforming its CrN_4 (507.9 mAh·g^{-1}, 0.039 % per cycle) and NC (288 mAh·g^{-1}, 0.053% per cycle) counterparts (Fig. 6(g)). The steady Coulombic efficiency close to unity also manifests excellent redox reversibility in the CrN_3-based configuration. Post-cycling SEM images were further collected. The CrN_3 electrode after charging (Figs. S23(a)–S23(f) in the ESM) displays uniform sulfur deposition, indicating excellent structural stability and effective suppression of sulfur agglomeration in contrast to those of the CrN_4 and NC electrodes. Moreover, SEM images after full discharge (Figs. S23(g)–S23(i) in the ESM) also reveal distinct Li_2S deposition across the different electrodes. The CrN_3 electrode features typical 3D Li_2S deposition, which facilitates efficient electron/ion transport. In comparison, the CrN_4 electrode displays a mixed 2D/3D deposition pattern, while the NC electrode is dominated by planar 2D Li_2S deposition, consistent with their sluggish redox kinetics and faster capacity decay. Overall, CrN_3 delivers outstanding cycling and rate performance, outperforming the conventional CrN_4 configuration and ranking competitively among state-of-the-art SAC-based systems (Fig. 6(h) and Table S3 in the ESM), affirming the significant advantage of undercoordination design in accelerating sulfur redox kinetics and improving LSB performance.

To further elucidate these electrochemical advancements, *operando* Raman spectroscopy was employed to monitor the evolution of sulfur species during cell cycling (Fig. 7(a)). The Raman contour plots for the CrN_3 and CrN_4 cells as a function of charge and discharge depth were depicted in Fig. 7(b). As the discharge initiates, distinct Raman bands emerge and intensify around 400, 450, and 510 cm^{-1}, corresponding to the formation and accumulation of S_6^{2-}, S_4^{2-}/S_5^{2-}, and S_8^{2-} species, respectively [40–42]. Continued discharge leads to suppression of these signals, attributed to the reduction of high-order LPSs into insoluble Li_2S_2/Li_2S, which deposit onto the electrode surface. During the subsequent charging process, these LPS signals reappear and reach a maximum before diminishing sharply near full charge, reflecting their oxidation to the element sulfur. By comparison, these LPS species in the CrN_3 configuration accumulate predominantly near the end of the upper discharge plateau and become nearly undetectable during later discharging, whereas CrN_4 witnesses a significantly prolonged presence of these intermediates. This strongly indicates that CrN_3 significantly accelerates both the

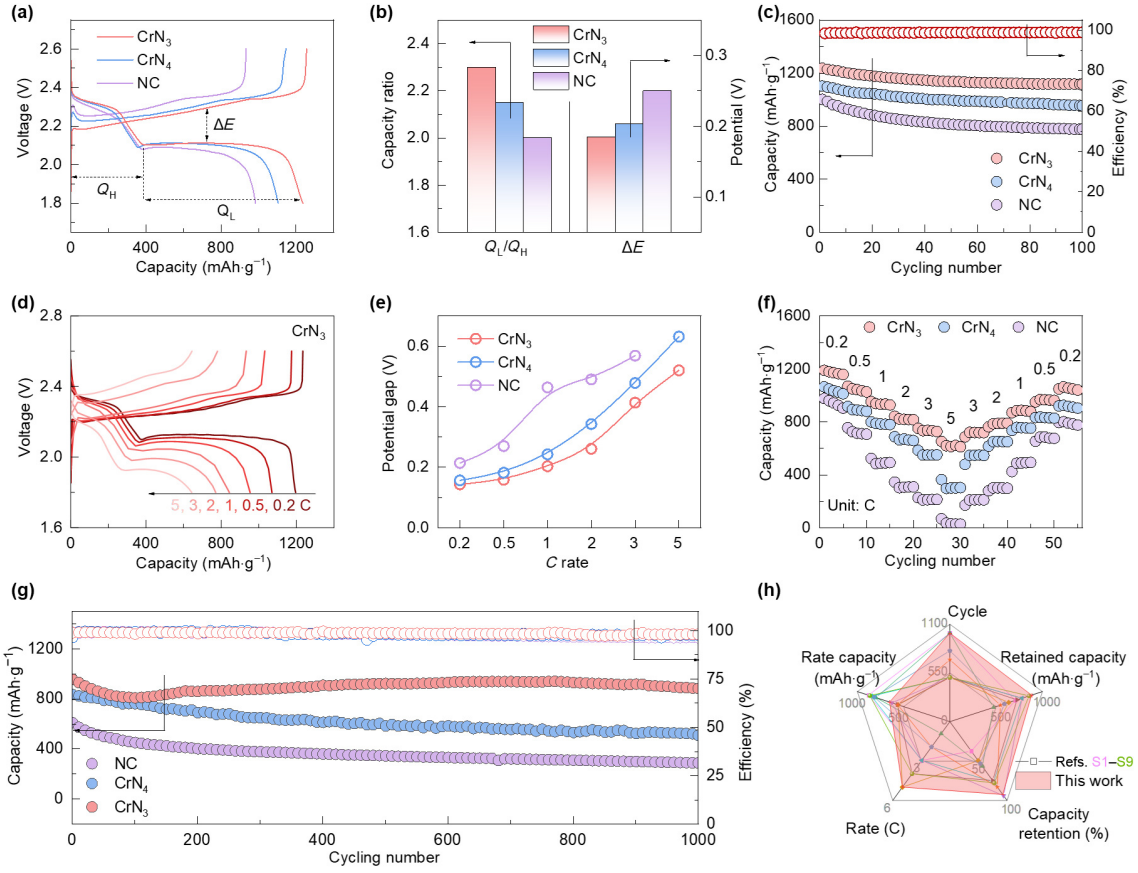

Figure 6 (a) Voltage profiles, (b) Q_L/Q_H and redox potential gaps, and (c) cycling performance at 0.2 C of LSBs based on CrN_3, CrN_4, and NC. (d) Voltage profiles of CrN_3 cell at various current rates. (e) Evolution of redox potential gaps along increasing current rate for different cells and (f) rate performance. (g) Long-term cycling performances of CrN_3, CrN_4, and NC cells at 1 C. (h) Performance comparison among CrN_3 cell and recently reported SAC-based LSBs.

generation and subsequent reduction of LPSs. Similarly, CrN_3 facilitates rapid oxidation of LPSs near the end of charging, in contrast to the persistent presence of LPSs throughout the charging period in the case of CrN_4. These observations further evidenced the superior catalytic efficacy of the undercoordinated CrN_3 catalyst in promoting fast and reversible sulfur redox conversions.

Based on these improvements, LSB performance under high sulfur loading and limited electrolyte was further explored to assess practical viability. When raising the sulfur loading to 3.0 mg·cm^{-2}, the CrN_3 cell still delivers a high specific capacity of 1069.8 mAh·g^{-1}, corresponding to an areal capacity of 3.21 mAh·cm^{-2}, and maintains stability during cycling (Fig. S24 in the ESM). Figure 7(c) compares the cycling performances of the CrN_3 and CrN_4 cells under more demanding conditions, i.e., a sulfur loading of 5.5 mg·cm^{-2} and a low electrolyte-to-sulfur ratio (E/S) of 5 mL·g^{-1}. Impressively, the CrN_3 cell achieves an areal capacity of 5.53 and retains 4.62 mAh·cm^{-2} after 50 cycles, substantially outperforming the CrN_4 counterpart (4.18 and 2.94 mAh·cm^{-2}, respectively) and the commercial LIB benchmark (~ 4.0 mAh·cm^{-2}), and exhibiting good competitiveness among recent reports based on SAC designs (Table S4 in the ESM). This highlights the exceptional catalytic capability of the undercoordinated CrN_3 design in sustaining high redox efficiency and reversibility under harsh operating conditions, which can be further validated by the significantly suppressed potential hysteresis in the voltage profile (Fig. 7(d)). Given this, pouch cells incorporating the CrN_3 catalyst were fabricated and successfully powered a cellphone (Fig. 7(e)), demonstrating its good potential for the development of practically viable LSBs. Based on the comprehensive analysis above, the mechanistic framework of undercoordination-enhanced sulfur electrochemistry is illustrated in Fig. 7(f). In contrast to the conventional CrN_4 coordination, the undercoordination in CrN_3 increases the Cr 3d electron density, which in turn intensifies the antibonding state occupancy upon hybridization with S 3p orbital, and moderately weakens LPS adsorbability. Meanwhile, this electronic regulation activates Cr in-plane orbital orientals for interacting with polysulfides, significantly facilitating charge transfer and lowering energy barriers for bidirectional sulfur redox. As a result, CrN_3 promotes faster reaction kinetics and superior redox reversibility, driving notable improvements in cyclability, rate capability, and high-loading performance.

3 Conclusion

In summary, we have developed a unique undercoordinated CrN_3 single-atom catalyst for boosting LSB performance. By employing a 2D layered ZIF precursor, we successfully lowered the coordination number of the single-atom moieties (CrN_3), in contrast to the conventional CrN_4 formed from the particulate ZIF-8-based precursor. The resulting 2D porous matrix facilitates efficient exposure of active surfaces and improves accessibility to mass/ion supplies, while the undercoordination slightly lowers 3d orbital occupancy and activates in-plane orbital orientations, leading to moderate LPS adsorption and reduced energy barriers for bidirectional sulfur conversions. As a result, fast and durable sulfur

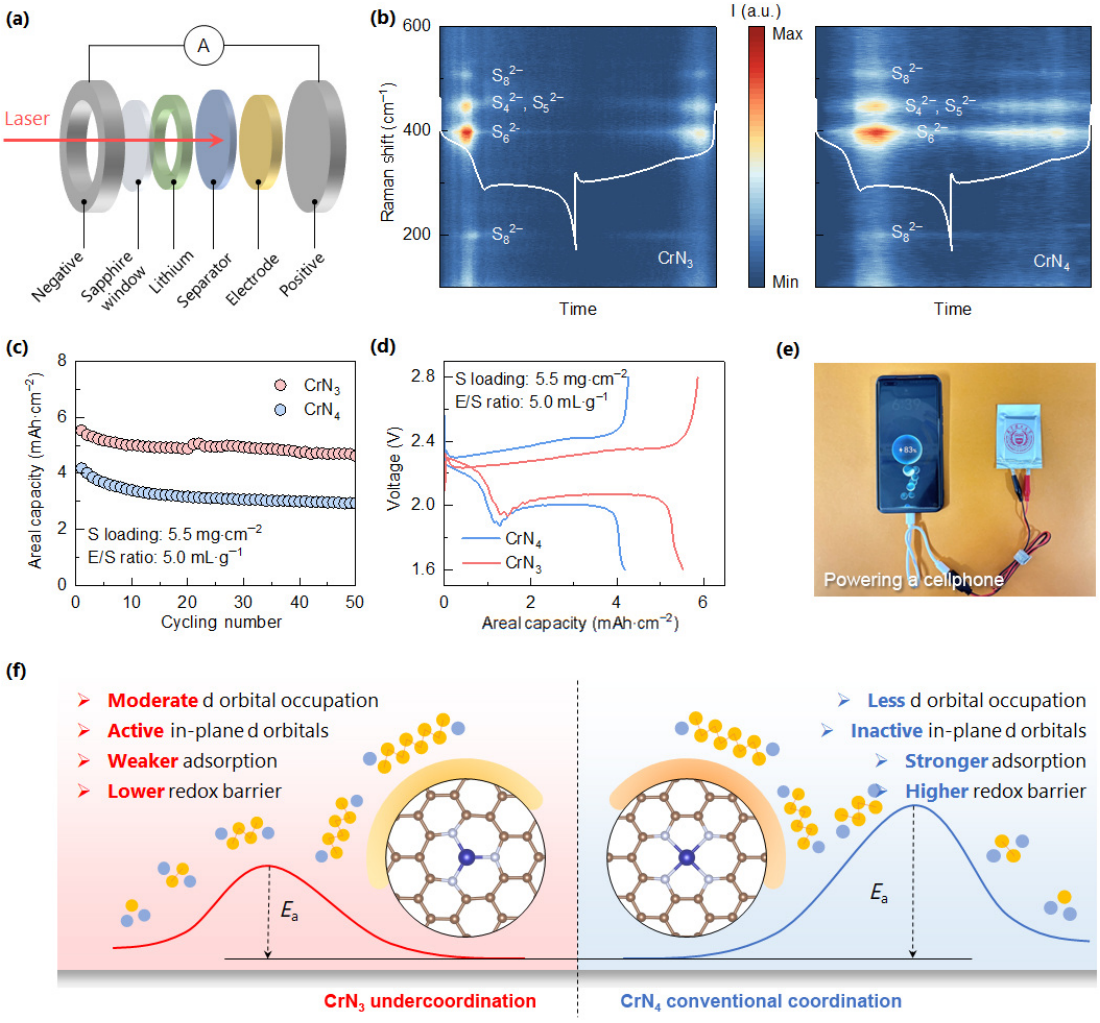

Figure 7 (a) Schematic of the setup for *operando* Raman measurement. (b) *Operando* Raman spectra of CrN_3 and CrN_4 cells. (c) Cycling performance and (d) voltage profiles of CrN_3 and CrN_4 cells under a sulfur loading of 5.5 mg·cm^{-2} and an E/S ratio of 5.0 mL·g^{-1}; (e) photograph of CrN_3-based pouch cell powering a cellphone; (f) schematic of advancing mechanism of undercoordination design.

electrochemistry was achieved, exhibiting excellent cyclability over 1000 cycles and commendable rate capability of up to 5 C, outperforming CrN_4 and many recently reported SACs. Even under challenging conditions of high sulfur loading (5.5 mg·cm^{-2}) and lean electrolyte (E/S = 5.0 mL·g^{-1}), CrN_3 still ensures robust sulfur redox activity, delivering a high areal capacity of 5.53 mAh·cm^{-2} that exceeds the commercial LIB benchmark. This work provides an effective and insightful strategy for rational coordination engineering in SACs, with broad potential to advance next-generation energy storage and conversion systems.

Electronic Supplementary Material: Supplementary material (the preparation and characterization methods of catalysts and electrodes, as well as the characterization of materials including XRD, SEM, adsorption configurations, electrochemical tests, etc.) is available in the online version of this article at https://doi.org/10.26599/NR.2025.94907915.

Data availability

All data needed to support the conclusions in the paper are presented in the manuscript and the Electronic Supplementary Material. Additional data related to this paper may be requested from the corresponding author upon request.

Acknowledgements

The authors thank the financial support from the National Natural Science Foundation of China (No. 22379069) and Fundamental Research Funds for the Central Universities (No. 30922010304).

Declaration of competing interest

All the contributing authors report no conflict of interest in this work.

Author contribution statement

H. Y. L.: Writing – original draft, review & editing, investigation, methodology, data curation, formal analysis. J. J. Z.: Writing – original draft, review & editing, investigation, formal analysis, validation. Y. R. D.: Writing – review & editing. Z. P. H.: Writing – review & editing. P. S. Q.: Writing – review & editing. F. Y. S.: Writing – review & editing. H. M. W.: Writing – review & editing, validation. G. R. L.: Conceptulization, project administration,

resources, supervision, validation, writing – review & editing. All the authors have approved the final manuscript.

Use of AI statement

None.

References

[1] Van Noorden, R. The rechargeable revolution: A better battery. *Nature* **2014**, *507*, 26–28.

[2] Bruce, P. G.; Freunberger, S. A.; Hardwick, L. J.; Tarascon, J. M. Li-O_2 and Li-S batteries with high energy storage. *Nat. Mater.* **2012**, *11*, 19–29.

[3] Hu, X. S.; Xu, L.; Lin, X. K.; Pecht, M. Battery lifetime prognostics. *Joule* **2020**, *4*, 310–346.

[4] Service, R. F. Lithium-sulfur batteries poised for leap. *Science* **2018**, *359*, 1080–1081.

[5] Conder, J.; Bouchet, R.; Trabesinger, S.; Marino, C.; Gubler, L.; Villevieille, C. Direct observation of lithium polysulfides in lithium-sulfur batteries using *operando* X-ray diffraction. *Nat. Energy* **2017**, *2*, 17069.

[6] Pang, Q.; Liang, X.; Kwok, C. Y.; Nazar, L. F. Advances in lithium-sulfur batteries based on multifunctional cathodes and electrolytes. *Nat. Energy* **2016**, *1*, 16132.

[7] Zhou, S. Y.; Shi, J.; Liu, S. G.; Li, G.; Pei, F.; Chen, Y. H.; Deng, J. X.; Zheng, Q. Z.; Li, J. Y.; Zhao, C. et al. Visualizing interfacial collective reaction behaviour of Li-S batteries. *Nature* **2023**, *621*, 75–81.

[8] Huang, Z. F.; Jaumaux, P.; Sun, B.; Guo, X.; Zhou, D.; Shanmukaraj, D.; Armand, M.; Rojo, T.; Wang, G. X. High-energy room-temperature sodium-sulfur and sodium-selenium batteries for sustainable energy storage. *Electrochem. Energy Rev.* **2023**, *6*, 21.

[9] Raza, H.; Bai, S. Y.; Cheng, J. Y.; Majumder, S.; Zhu, H.; Liu, Q.; Zheng, G. P.; Li, X. F.; Chen, G. H. Li–S batteries: Challenges, achievements and opportunities. *Electrochem. Energy Rev.* **2023**, *6*, 29.

[10] Zhuang, Z. C.; Kang, Q.; Wang, D. S.; Li, Y. D. Single-atom catalysis enables long-life, high-energy lithium-sulfur batteries. *Nano Res.* **2020**, *13*, 1856–1866.

[11] Zhang, S. L.; Ao, X.; Huang, J.; Wei, B.; Zhai, Y. L.; Zhai, D.; Deng, W. Q.; Su, C. L.; Wang, D. S.; Li, Y. D. Isolated single-atom Ni–N_5 catalytic site in hollow porous carbon capsules for efficient lithium-sulfur batteries. *Nano Lett.* **2021**, *21*, 9691–9698.

[12] Zhang, E. H.; Hu, X.; Meng, L. Z.; Qiu, M.; Chen, J. X.; Liu, Y. J.; Liu, G. Y.; Zhuang, Z. C.; Zheng, X. B.; Zheng, L. R. et al. Single-atom yttrium engineering janus electrode for rechargeable Na–S batteries. *J. Am. Chem. Soc.* **2022**, *144*, 18995–19007.

[13] Zhao, Y.; Qiao, W. J.; Wang, H. Z.; Xie, Y. Y.; Teng, B. T.; Li, J. R.; Sun, Y. L.; Alsubaie, A. S.; Wan, T.; El-Bahy, S. M. et al. Introducing phosphoric acid to fluorinated polyimide towards high performance laser induced graphene electrodes for high energy micro-supercapacitors. *Carbon* **2024**, *230*, 119665.

[14] Fang, R. P.; Chen, K.; Yin, L. C.; Sun, Z. H.; Li, F.; Cheng, H. M. The regulating role of carbon nanotubes and graphene in lithium-ion and lithium-sulfur batteries. *Adv. Mater.* **2019**, *31*, 1800863.

[15] Li, H. Y.; Cai, B.; Song, Y. Z.; Cai, W. L.; Li, G. R. Bidirectionally polarizing surface chemistry of heteroatom-doped carbon matrix towards fast and longevous lithium-sulfur batteries. *Chin. Chem. Lett.* **2023**, *34*, 107811.

[16] Qin, J. L.; Wang, R.; Yuan, Z. L.; Xiao, P.; Wang, D. L. Manipulating fast Li_2S redox via carbon confinement and oxygen defect engineering of In_2O_3 for lithium-sulfur batteries. *Nano Res.* **2024**, *17*, 5179–5187.

[17] Zhen, M. M.; Jiang, K. L.; Guo, S. Q.; Shen, B. X.; Liu, H. L. Suitable lithium polysulfides diffusion and adsorption on CNTs@TiO_2-Bronze nanosheets surface for high-performance lithium-sulfur batteries. *Nano Res.* **2022**, *15*, 933–941.

[18] Zhou, G. M.; Tian, H. Z.; Jin, Y.; Tao, X. Y.; Liu, B. F.; Zhang, R. F.; She, Z. W.; Zhuo, D.; Liu, Y. Y.; Sun, J. et al. Catalytic oxidation of Li_2S on the surface of metal sulfides for Li-S batteries. *Proc. Natl. Acad. Sci. USA* **2017**, *114*, 840–845.

[19] Wu, G. Z.; Li, S. Q.; Chen, Z.; Sun, A. J.; Yang, J.; Joo, S. W.; Huang, J. R. MoP nanoparticles encapsulated in N-doped carbon nanotubes as sulfur host for advanced lithium-sulfur batteries. *Nano Res.* **2024**, *17*, 2736–2745.

[20] Jiang, H. Q.; Liu, X. C.; Wu, Y. S.; Shu, Y. F.; Gong, X.; Ke, F. S.; Deng, H. X. Metal-organic frameworks for high charge-discharge rates in lithium-sulfur batteries. *Angew. Chem., Int. Ed.* **2018**, *57*, 3916–3921.

[21] Hu, X. H.; Jian, J. H.; Fang, Z. S.; Zhong, L. F.; Yuan, Z. K.; Yang, M. J.; Ren, S. J.; Zhang, Q.; Chen, X. D.; Yu, D. S. Hierarchical assemblies of conjugated ultrathin COF nanosheets for high-sulfur-loading and long-lifespan lithium-sulfur batteries: Fully-exposed porphyrin matters. *Energy Storage Mater.* **2019**, *22*, 40–47.

[22] Wei, C. L.; Wang, Y. S.; Zhang, Y. C.; Tan, L. W.; Qian, Y.; Tao, Y.; Xiong, S. L.; Feng, J. K. Flexible and stable 3D lithium metal anodes based on self-standing MXene/COF frameworks for high-performance lithium-sulfur batteries. *Nano Res.* **2021**, *14*, 3576–3584.

[23] Li, G. R.; Zhang, J. J.; Wu, Z. Z.; Li, H. Y.; Song, Y. Z.; Zhang, S. Q. Local structure modulations of single-atom catalysts in sulfur electrocatalysis: A comprehensive review. *Mater. Today* **2025**, *85*, 141–170.

[24] Wang, Z. W.; Cheng, Y. W.; Wang, S. Y.; Xu, J.; Peng, B.; Luo, D.; Ma, L. B. Promoting polysulfide conversions via cobalt single-atom catalyst for fast and durable lithium-sulfur batteries. *Nano Res.* **2023**, *16*, 9335–9343.

[25] Han, Z. Y.; Zhao, S. Y.; Xiao, J. W.; Zhong, X. W.; Sheng, J. Z.; Lv, W.; Zhang, Q. F.; Zhou, G. M.; Cheng, H. M. Engineering d-p orbital hybridization in single-atom metal-embedded three-dimensional electrodes for Li–S batteries. *Adv. Mater.* **2021**, *33*, 2105947.

[26] Liang, Z. W.; Shen, J. D.; Xu, X. J.; Li, F. K.; Liu, J.; Yuan, B.; Yu, Y.; Zhu, M. Advances in the development of single-atom catalysts for high-energy-density lithium-sulfur batteries. *Adv. Mater.* **2022**, *34*, 2200102.

[27] Zhang, T. Q.; Chen, Z.; Zhao, J. X.; Ding, Y. H. Metal-N_4/graphene as an efficient anchoring material for lithium-sulfur batteries: A computational study. *Diam. Relat. Mater.* **2018**, *90*, 72–78.

[28] Zhou, R.; Gu, S. N.; Guo, M.; Xu, S. Z.; Zhou, G. W. Progresses and prospects of asymmetrically coordinated single atom catalysts for lithium-sulfur batteries. *Energy Environ. Mater.* **2024**, *7*, e12703.

[29] Luo, J. M.; Zhang, Y. T.; Lu, Z.; Liu, C.; Xu, Y. S.; Chen, H.; Wang, Q.; Wu, D. X.; Dang, D.; Deng, Y. J. et al. Oxygen-coordinated Cr single-atom catalyst for oxygen reduction reaction in proton exchange membrane fuel cells. *Angew. Chem., Int. Ed.* **2025**, *64*, e202500500.

[30] Yang, D. W.; Wang, J. A.; Lou, C. J.; Li, M. Y.; Zhang, C. Q.; Ramon, A.; Li, C. H.; Tang, M. X.; Henkelman, G.; Xu, M. et al. Single-atom catalysts with unsaturated Co-N_2 active sites based on a C_2N 2D-organic framework for efficient sulfur redox reaction. *ACS Energy Lett.* **2024**, *9*, 2083–2091.

[31] Li, S.; Li, L. B.; Zhao, Y. M. Y.; Yang, H.; Tong, H.; Fan, S. B.; Wang, Z. X.; Xu, W. H. Modulating the d-band center of single-atom catalysts for efficient Li_2S_2-Li_2S conversion in durable lithium-sulfur batteries. *Energy Storage Mater.* **2024**, *70*, 103477.

[32] Li, H. Y.; Chen, G. X.; Zhang, K. L.; Wang, L. B.; Li, G. R. Dually sulphophilic chromium boride nanocatalyst boosting sulfur conversion kinetics toward high-performance lithium-sulfur batteries. *Adv. Sci.* **2023**, *10*, 2303830.

[33] Li, H. Y.; Huang, Z. P.; Qian, P. S.; Wang, Y. Q.; Gao, R.; Bendounan, A.; Wang, H. M.; Chen, Z. S.; Zeng, H. B.; Li, G. R.

Phosphorus-tuned nickel boride nanocatalyst with enhanced *p-p* interaction for expediting sulfur electrochemistry in lithium-sulfur batteries. *Adv. Funct. Mater.* **2025**, *35*, 2419837.

[34] Zhang, F. C.; Tang, Z. H.; Zhang, T. F.; Xiao, H.; Zhuang, H. F.; Han, P. Y.; Zheng, L. R.; Jiang, L.; Gao, Q. M. Electronic modulation and symmetry-breaking engineering of single-atom catalysts driving long-cycling Li–S battery. *Angew. Chem., Int. Ed.* **2025**, *64*, e202418749.

[35] Tian, S. H.; Liu, G.; Xu, S. X.; Han, C.; Tao, K.; Huang, J. J.; Peng, S. L. Deposition mode design of Li_2S: Transmitted orbital overlap strategy in highly stable lithium-sulfur battery. *Adv. Funct. Mater.* **2024**, *34*, 2309437.

[36] Li, G. R.; Qiu, W. L.; Gao, W. J.; Zhu, Y. J.; Zhang, X. M.; Li, H. Y.; Zhang, Y. G.; Wang, X.; Chen, Z. W. Finely-dispersed Ni_2Co nanoalloys on flower-like graphene microassembly empowering a bi-service matrix for superior lithium-sulfur electrochemistry. *Adv. Funct. Mater.* **2022**, *32*, 2202853.

[37] Luo, C.; Liang, X.; Sun, Y. F.; Lv, W.; Sun, Y. W.; Lu, Z. Y.; Hua, W. X.; Yang, H. T.; Wang, R. C.; Yan, C. L. et al. An organic nickel salt-based electrolyte additive boosts homogeneous catalysis for lithium-sulfur batteries. *Energy Storage Mater.* **2020**, *33*, 290–297.

[38] Zhang, X.; Li, X. Y.; Zhang, Y. Z.; Li, X.; Guan, Q. H.; Wang, J.; Zhuang, Z. C.; Zhuang, Q.; Cheng, X. M.; Liu, H. T. et al. Accelerated Li^+ desolvation for diffusion booster enabling low-temperature sulfur redox kinetics via electrocatalytic carbon-grazfted-CoP porous nanosheets. *Adv. Funct. Mater.* **2023**, *33*, 2302624.

[39] Chen, G. X.; Li, H. Y.; Wang, Y. Q.; Ding, Y. R.; Qian, P. S.; Zhang, K. L.; Zeng, H. B.; Li, G. R. Ultrafine iron boride as a highly efficient nanocatalyst expedites sulfur redox electrochemistry for high-performance lithium-sulfur batteries. *Batter. Supercaps* **2024**, *7*, e202400128.

[40] Ye, X.; Wu, F.; Xue, Z. Y.; Yuan, H. W.; Mei, S. J.; Wang, J. C.; Yang, R. Z.; Wu, X. M.; Zhao, X. L.; Pan, H. et al. Accelerated polysulfide conversion by rationally designed NiS_2-CoS_2 heterostructure in lithium-sulfur batteries. *Adv. Funct. Mater.* **2025**, *35*, 2417776.

[41] Wu, X. P.; Xie, R. J.; Cai, D. P.; Fei, B.; Zhang, C. Q.; Chen, Q. D.; Sa, B.; Zhan, H. B. Engineering defect-rich bimetallic telluride with dense heterointerfaces for high-performance lithium-sulfur batteries. *Adv. Funct. Mater.* **2024**, *34*, 2315012.

[42] Xu, H. F.; Jiang, Q. B.; Hui, K. S.; Wang, S.; Liu, L. W.; Chen, T. Y.; Zheng, Y. S.; Ip, W. F.; Dinh, D. A.; Zha, C. et al. Interfacial "double-terminal binding sites" catalysts synergistically boosting the electrocatalytic Li_2S redox for durable lithium-sulfur batteries. *ACS Nano* **2024**, *18*, 8839–8852.